



A novel hybrid $\text{Bi}_2\text{MoO}_6\text{-MnO}_2$ catalysts with the superior plasma induced pseudo photocatalytic-catalytic performance for ethyl acetate degradation

Haiqiang Wang^{a,b}, Si Chen^{a,b}, Zhi Wang^{a,b}, Yi Zhou^{a,b}, Zhongbiao Wu^{a,b,*}

^a Key Laboratory of Environment Remediation and Ecological Health, Ministry of Education, College of Environmental & Resources Science, Zhejiang University, Hangzhou, 310058, PR China

^b Zhejiang Provincial Engineering Research Center of Industrial Boiler & Furnace Flue Gas Pollution Control, Hangzhou, 310027, PR China



ARTICLE INFO

Keywords:
 $\text{Bi}_2\text{MoO}_6\text{-MnO}_2$
 Plasma
 Ethyl acetate
 Catalytic degradation
 Synergetic effect

ABSTRACT

A hybrid catalyst system of $\text{Bi}_2\text{MoO}_6\text{-MnO}_2$ was designed and applied in a plasma system for the degradation of ethyl acetate (EA). This hybrid catalyst greatly improved the utilization of plasma-generated species like high-energy electrons, O and O_3 . In addition, an excellent removal efficiency of EA (100%), selectivity of CO_2 (70%) and selectivity of CO_x (99%) at a specific input energy of 392 J/L were achieved compared to the pure catalyst materials or plasma alone. The enhanced discharge intensity of the plasma, adsorption capability for EA, and oxidation capability of the hybrid catalyst in plasma made simultaneous contributions to this improved performance. A synergetic effect between Bi_2MoO_6 and MnO_2 evidently occurred, showing that h^+ generated from Bi_2MoO_6 by “pseudo photocatalysis” can induce the transformation of Mn^{3+} to Mn^{4+} of MnO_2 in plasma. Further, Fourier transform infrared (FT-IR) spectra and gas chromatography mass spectrometry (GC-MS) results indicated that the degradation of EA firstly took place on the surface of the hybrid $\text{Bi}_2\text{MoO}_6\text{-MnO}_2$ catalyst in the plasma environment, along with the formation of by-products like acetic acid, acetone and CH_4 . Then, the by-products were converted to CO_x by the oxidation of O_3 . This novel strategy of integrating the contributions of photocatalyst and thermocatalyst in a plasma environment described in this work should inspire the rational design of more catalysts for plasma-catalyst systems for the purification of environmental pollutants.

1. Introduction

Plasma is a system that selectively transfers the input energy to electrons, after which those high-energy electrons (e^*) collide gas molecules to form active radicals (O, N, O_3), that can react with and degrade pollutants [1,2]. However, the ideal utilization efficiency of those high energy species basically cannot be achieved within a single plasma system, leading to incomplete oxidation of pollutants and the formation of toxic by-products, as well as the waste of electrical energy [3]. Using suitable catalysts in a plasma environment to combine two methods of pollutant degradation is an interesting idea and may be able to overcome this hindrance of the application of plasma. Thus, hybrid systems of plasma and catalysts have gained extensive attention recently [4,5]. It is expected that the added catalysts can take full advantage of those plasma-generated species, which will greatly enhance the utilization efficiency of the input energy, along with the total degradation of pollutants. Therefore, designing a catalyst that specifically fits the characteristic of the plasma discharge is an important challenge in the

realization of the combination of plasma and catalyst.

It is also well known that packing beads or catalyst particles in the discharge zone would lead to changes in the electric field distribution as well as the discharge behavior. Thus, a better efficiency may be obtained with an improved discharge intensity after adding catalysts [6,7]. Besides, nanomaterials with micro- and mesoporous structures exhibits excellent adsorption of pollutants which plays a vital role in the catalytic degradation process. Thus, it is also important to take full account of the physical properties of nano-catalysts, due to their effect on the status of the plasma discharge and their pollutant adsorption capability to pollutants.

Bi_2MoO_6 , a typical n-type semiconductor with a suitable band gap energy (E_g) of about 2.2–2.5 eV, has been widely employed in photocatalysis processes [8,9]. It can be activated to produce electron-hole ($e^- \text{-} h^+$) pairs and some derived species like superoxide radicals (O_2^-) and hydroxyl radicals ($\cdot\text{OH}$), showing strong oxidability to volatile organic compounds (VOCs), when the energy of the absorbed photon is greater than its E_g [10–12]. Similarly, it can also be activated by the

* Corresponding author at: Key Laboratory of Environment Remediation and Ecological Health, Ministry of Education, College of Environmental & Resources Science, Zhejiang University, Hangzhou, 310058, PR China.

E-mail address: zbwu@zju.edu.cn (Z. Wu).

collision of e^* in plasma to realize a “pseudo photocatalysis” behavior, since the energy of e^* is 1–25 eV, just covering the requirement of semiconductors to be activated, as reported in our previous study [13]. Under these condition, e^* can be realize its best contribution, and a highly enhanced energy utilization efficiency can be obtained and the removal efficiency will also be increased. Besides, Bi_2MoO_6 with a self-assembled hollow-microsphere structure on nanosheets will not only be helpful to the propagation of filamentary discharge on the surface of the catalysts, and facilitate the discharge process, but it will also benefit the discharge stability of the plasma process. In addition, it has been reported to exhibit great adsorption capability for VOCs as reported [14]. Therefore, it will be a good candidate to use as the catalyst in a plasma discharge system.

However, the utilization of O_3 , which is one of the most pressing environmental issues, as O_3 would inevitably be generated in the plasma discharge process, is still an obstacle for the simple Bi_2MoO_6 system [1]. Other catalyst components focused on the degradation and utilization of O_3 should be considered simultaneously, to further enhance both the utilization of plasma generated species and the degradation of VOCs. It is well known that MnO_2 can efficiently decompose O_3 into reactive oxygen species, and consequently facilitates the degradation of VOCs [15–17]; MnO_2 therefore, meets our needs. Besides, the temperature in the plasma will increase slightly with discharge time [18], so it is possible that MnO_2 can be activated. Thus MnO_2 , a traditional thermocatalyst, may also play a part in plasma discharge systems, due to its wonderful redox property.

Volatile organic compounds (VOCs), a serious issue for atmospheric pollution and human health, urgently need to be addressed and has attracted more attention [19,20]. In this paper, ethyl acetate (EA), a typical VOCs [21], was selected as the probe pollutant. Bi_2MoO_6 and MnO_2 were firstly integrated as a hybrid catalyst system, and then used in a plasma discharge environment for the degradation of EA, with the goal of realizing the best possible energy utilization of the plasma process. X-ray diffraction (XRD), scanning electron microscopy (SEM), transmission electron microscopy (TEM), Brunauer–Emmett–Teller (BET) adsorption, CO plasma-process reduction (CO-PPR), and X-ray photoelectron spectroscopy (XPS) were used for the characterization of the catalysts, gas chromatography mass spectrometry (GC-MS) was employed for the detection of by-products, and Fourier transform infrared (FT-IR) spectroscopy was used to clarify the reaction pathways. The removal efficiency of EA, the selectivity of CO_x and the generation of by-products were studied. Together, the discharge intensity of the plasma, the adsorption capability for EA and the oxidation capability of the hybrid catalyst in the plasma discharge process were investigated to explore the relationship between the hybrid catalyst and plasma and the plasma catalytic degradation mechanism of EA.

2. Experimental

2.1. Experimental setup

Figure S1 displays a diagram illustrating the complete experimental system. A dual dielectric coaxial dielectric barrier discharge (DBD) reactor with a discharge gap of 3.5 mm and discharge length of 200 mm was employed. Stainless steel wire tightly wound around a quartz tube with an inner diameter of 20 mm and thickness of 5 mm was used as high-voltage electrode. A ceramic tube filled with metal powder was located on the axis of the quartz tube with an outer diameter of 13 mm, while the ground electrode was the metal powder. Catalysts (1–2 g) coated onto the glass balls (36 g) were packed in the discharge zone. Reaction feed consisted of 200 ± 5 ppm EA, 2.82 L/min N_2 , and 180 mL/min O_2 , while gaseous EA was supplied by feeding a dry N_2 flow (7.2 mL/min) through liquid EA (99.9%, Sinopharm Chemical Reagent Co., Ltd) which were contained in a bubbler in a water bath (20°C). Other three VOCs (Toluene, Acetone and P-xylene) with inlet concentration of 200 ± 5 ppm were chosen for activity tests under the

same conditions.

The concentration of EA and CO_2/CO production were analyzed online by a gas chromatograph (GC, FULI9790II, China) equipped with a flame ionization detector (FID), an electron capture detector (ECD) and nickel converting equipment. The removal efficiency of EA and the selectivity of $\text{CO}_x/\text{CO}/\text{CO}_2$ were defined as:

$$\eta_{\text{C4H8O2}} = \frac{C_{\text{inlet}} - C_{\text{outlet}}}{C_{\text{inlet}}} \times 100\% \quad (1)$$

$$\text{COx selectivity}(\%) = \frac{C_{\text{CO}} + C_{\text{CO}_2}}{(C_{\text{inlet}} - C_{\text{outlet}}) \times 4} \times 100\% \quad (2)$$

$$\text{CO selectivity}(\%) = \frac{C_{\text{CO}}}{(C_{\text{inlet}} - C_{\text{outlet}}) \times 4} \times 100\% \quad (3)$$

$$\text{CO}_2 \text{ selectivity}(\%) = \frac{C_{\text{CO}_2}}{(C_{\text{inlet}} - C_{\text{outlet}}) \times 4} \times 100\% \quad (4)$$

A modulating pulse power of up to 500 W in the frequency range of 5–20 kHz, along with a duty cycle of 1–99% was provided by a power source from Nanjing Suman Plasma Technology Co. A digital oscilloscope (TDS2014C, Tektronix), high-voltage probe (P6015A, Tektronix), and current probe (CP8030B, Zhiyong) were employed to measure the waveform, voltage, and current, respectively. The duty ratio and the modulation frequency of the modulating pulse power source were fixed at 60% and 64 Hz for all tests, respectively. The correlation between applied voltage and specific input energy (SIE) were shown in Table S1. The SIE, the average current and effective current were defined and calculated as follows:

$$\text{SIE (J/L)} = P/Q = \text{discharge power (W)} \times 60 \text{ (s/min)} / \text{total flow rate (L/min)} \quad (5)$$

$$P (\text{W}) = E \times f = \text{input energy (J)} \times \text{frequency (Hz)} \quad (6)$$

$$E (\text{J}) = \int_0^T u(t) \times i(t) dt = \int_0^{\text{one pulse time}} \text{transient voltage (V)} \times \text{transient current (A)} dt \quad (7)$$

$$\text{Average current (A)} = \int_0^T |i(t)| dt / t \quad (8)$$

$$\text{Effective current (A)} = \int_0^T (i(t))^2 dt / t \quad (9)$$

2.2. Catalysts preparation

Preparation of MnO_2 . As reported in the literature [22], KMnO_4 (2.37 g) was immersed in 150 mL of a 0.4 M acetic acid solution. After vigorous stirring for 4 h, the mixture was transferred to a 200 mL Teflon-lined autoclave and maintained at 140°C for 12 h. The obtained solid products were collected by filtration, washed with deionized water and absolute ethanol, and then dried at 70°C .

Preparation of flower-like $\text{Bi}_2\text{MoO}_6/\text{MnO}_2$. Different mole ratios (from 1:1 to 4:1) of $\text{Bi}_2\text{MoO}_6/\text{MnO}_2$ were synthesized using the process reported in the literature [23] with little modification and denoted as BMO-Mn (x:1, where x was 1, 2 and 4). $\text{Bi}(\text{NO}_3)_3 \cdot 5\text{H}_2\text{O}$ (5 mmol), $\text{Na}_2\text{MoO}_4 \cdot 5\text{H}_2\text{O}$ (2.5 mmol) and MnO_2 nanowire (0.625–2.5 mmol) were immersed in 50 mL of ethylene glycol, and then mixed together with further stirring for 30 min. The resulting suspension was maintained at 160°C for 24 h in a 200 mL Teflon-lined autoclave, and then allowed to cool to room temperature naturally. The claybank powders were collected by filtration, washed with deionized water and absolute ethanol several times, and then dried at 70°C . For comparison, pure flower-like Bi_2MoO_6 and solvothermal treated MnO_2 (denoted as Solvo- MnO_2) were also synthesized in the same way without the addition of MnO_2 and the precursor of Bi_2MoO_6 , respectively. In addition, solid Bi_2MoO_6 and MnO_2 with a mole ratio of 2:1 were mixed thoroughly and denoted as BMO-Mn (solid mix).

2.3. Characterizations

The crystal phases of the samples were verified using powder X-ray diffraction with Cu K α radiation at a wavelength of 0.15418 nm (model D/max RA, Rigaku Co., Japan). The data were collected by scanning over angles (2θ) ranging from 5° to 80° with a step size of 4°. Microscopic morphology and structure were characterized by scanning electron microscopy (SEM, HITACHI UHR FE-SEM, SU 8010) and transmission electron microscopy (TEM, H-600, Hitachi, Ltd., Japan, Voltage: 200kV). The specific surface area and pore structure were analyzed by the Brunauer–Emmett–Teller (BET) method using a nitrogen adsorption apparatus (JW-BK132F, China). XPS with a monochromatic Al K α source (150W, 1486.6 eV) was employed to study the surface properties and valence state distribution (Thermo ESCALAB 250, USA), and the C 1s level at 284.8 eV was regarded as an internal standard to revise the shift of the binding energy due to relative surface charging. A “modified CO temperature-programmed reduction (CO-TPR)” experiment was conducted in plasma to determine the oxidize ability of the catalysts in the plasma system by changing the factor of temperature to input energy of plasma. This technique is called “CO plasma-programmed reduction (CO-PPR)”. Equal amount of catalysts with activity tests were coated on glass balls and filled in the plasma zone. In each measurement, catalysts were pretreated in pure He for 1h (SIE = 0 J/L), and then discharged at different input energy in a CO atmosphere (4% CO/He) at a flow rate of 1L/min. A sample of discharging on blank glass balls without coating catalysts should be done as the background value. The yield of CO₂ was taken as the detection signal by using FT-IR (Bruker ALPHA-G, Germany).

2.4. By-products measurements

Fourier transform infrared spectroscopy (FT-IR) was applied to dynamically evaluate the types of by-products. Measurements were conducted by using a Bruker ALPHA-G spectrometer (Bruker, Germany) with a 0.5 L gas cell and a spectrum was obtained by overlapping 16 scans at a resolution of 4 cm⁻¹. O₃ was measured by an O₃ analyzer (UV-100, Eco Sensors in America).

A GC-MS system (GC: Agilent 7890A, MS: Agilent 5975C) equipped with a J&W113–4332GS-GasPro chromatographic column (America) was also employed to analyze the components of the off-gas (containing multiple gaseous products), which was captured by employing an adsorption tube (Tenax TA/Tenax GR) at room temperature for 1 h, and was then released in a thermal desorption instrument (TDI, PERSEE-TP7, PR China) at 300 °C and fed into the GC-MS system for analysis. The by-products deposited on the surface of the catalysts were also measured by using the GC-MS system. First, 0.1 g of used catalysts were packed into a quartz tube and held by quartz wool, then subjected to a thermal desorption at 300 °C to release the by-products and injected into the GC-MS system for analysis. The analysis process was consistent with the off-gas measurement.

3. Results and discussion

3.1. Structure, composition and morphology

The crystal structure and chemical composition of the as-prepared catalysts were characterized by XRD and XPS, respectively, as displayed in Fig. 1. The XRD pattern (Fig. 1a) of MnO₂ could be indexed to the pure crystal phase of α -MnO₂ (JCPDS Card No. 44-0141), whereas nearly no obvious diffraction peaks were found for Solvo-MnO₂, suggesting that its crystallinity may be destroyed and the compound became amorphous after the solvothermal treatment. Pure Bi₂MoO₆ exhibited an orthorhombic phase (JCPDS Card No. 76-2388) [24] with several strong characteristic peaks at $2\theta = 25.28^\circ$, 32.59° , 33.07° , 46.72° , 55.46° and 56.16° . As for the BMO-Mn hybrid catalyst, only distinctive peaks of Bi₂MoO₆ were observed, with no peaks attributed to

MnO₂, due to the amorphous form of MnO₂ in the prepared samples. In addition, the intensity of the peaks for Bi₂MoO₆ varied with its content, and the moderate addition of MnO₂ may be a benefit for the integrity of the Bi₂MoO₆ crystal structure (Fig. 1a₂). Furthermore, the presence of constituent elements of BMO-Mn containing Bi, Mo, O and Mn were identified from the survey scan during XPS analysis (Fig. 1b). Results from XRD and XPS confirmed the formation of hybrid catalyst materials without any impurities.

The microscale morphologies of the prepared samples were investigated using SEM and TEM images (Fig. 2). Pure Bi₂MoO₆ featured a “hydrangea-like” hollow-microsphere structure self-assembled from nanosheets, with a diameter of 2–3 μ m (Fig. 2a and e), and its interplanar spacing of 0.315 nm was verified by HRTEM (Fig. 2e₁ and e₂), corresponding to the (131) crystal planes. MnO₂ presented as nanowires with length of 1.6–2 μ m (Fig. 2b₁ and f), which exposed the (200) crystal planes with an interplanar spacing of 0.484 nm (Fig. 2f₁). While aggregation and destruction of its structure were brought about by the solvothermal treatment, the Solvo-MnO₂ exhibited loose and sponge-like shape with the bulk of amorphous particles (Fig. 2b and g), as suggested by the XRD results. Fig. 2c, d and h show micro-images of BMO-Mn (2:1) composites, where the amorphous particles of Solvo-MnO₂ were uniformly deposited on every sheet of the Bi₂MoO₆ spheres, indicating optimal contact between the two components. Note that the hybrid catalyst appeared distributed with feature alternate with brightness and darkness (Fig. 2h₂), exhibiting a unique morphology of densely populated pores [25]. EDX and an elemental map (Fig. S2) further confirmed the existence and distribution of the hybrid catalyst, with no other impurities observed.

3.2. EA degradation performance, selectivity and stability

The EA conversion as a function of input energy was investigated under the combination of plasma discharge and as-prepared catalysts (Fig. 3a), and the EA removal efficiency was found to increase monotonically with increasing input energy regardless of the existence of any catalysts. It is widely acknowledged that a higher discharge energy would facilitate the generation of more microdischarge and more active species (e.g. O, N and O₃) for chemical reactions [26]. The participation of catalysts in plasma discharge highly enhanced the degradation efficiency of EA, especially the hybrid catalysts. Over 90% EA conversion and nearly 100% EA conversion were obtained at 214 J/L and 322 J/L, respectively, for using the BMO-Mn catalysts, which was much higher than that obtained using either of the single catalysts of MnO₂ and Bi₂MoO₆ (56% and 47% at 214 J/L, 78% and 65% at 322 J/L, respectively) and the solid-mixed one (81% at 214 J/L and 92% at 322 J/L). These results indicated that the synergistic promotion of EA conversion took place due to the co-existence of MnO₂ and Bi₂MoO₆ in the plasma discharge. In addition, the performance of solvo-MnO₂ was good at low SIE, but became bad when SIE was larger than 200 J/L, compared to MnO₂. Furthermore, the activity of BMO-Mn increased rapidly as the mole ratio of Bi₂MoO₆/MnO₂ was increased, reached a peak value at Bi₂MoO₆/MnO₂ = 2:1, and then decreased. Possible reasons for this behavior are as follows: (A) Bi₂MoO₆, characterized as an n-type semiconductor, could be activated by high-energy electrons in the plasma to achieve a “pseudo photocatalysis” behavior, and then played an important role in pollutants degradation, as shown in our previous study [13]. Hence the increased molar ratio of Bi₂MoO₆ would facilitate the “pseudo photocatalysis” behavior. (B) When the molar ratio of Bi₂MoO₆ was too large (4:1), O₃ produced by the plasma may not be taken full advantage of (Fig. S3), and thus the removal of EA was inhibited, since MnO₂ acts as such a good catalyst for the degradation and utilization of O₃ [16,17]. Hence, the molar ratio of 2:1 would be the best choice and used in the following discussions.

As for the selectivity of by-products (Fig. c and c₁), both MnO₂ and solvo-MnO₂ exhibited incomplete CO₂ and CO_x conversion all the way, the peak values were 30% and 58% for MnO₂, 43% and 67% for solvo-

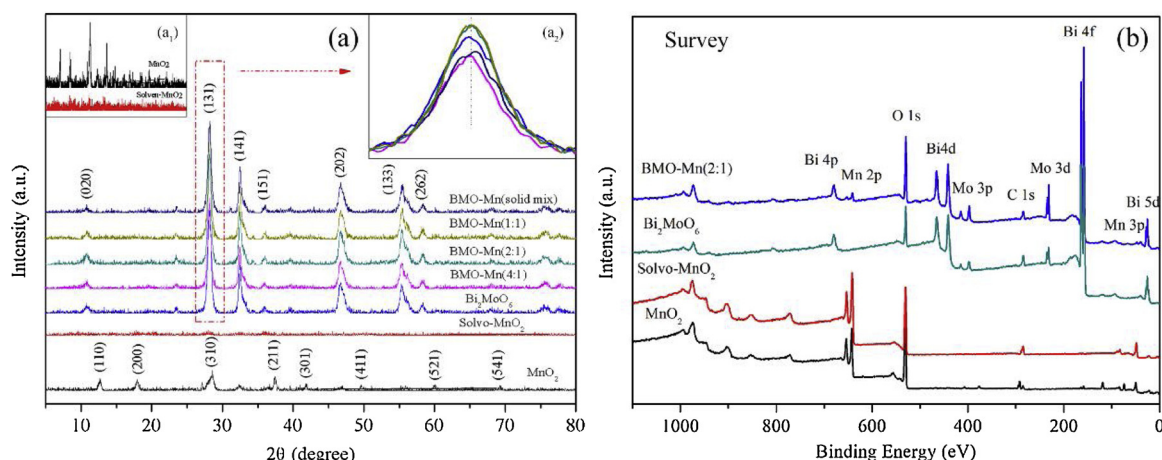


Fig. 1. (a) XRD pattern, (a₁) enlarged view of weak-signal XRD pattern of MnO₂ and Solvo-MnO₂, (a₂) enlarged view of the main (131) peak of Bi₂MoO₆. (b) XPS survey scan.

MnO₂, respectively, indicating that the solvothermal treatment may have induced some property change in the catalysts and enhanced the generation of CO_x, especially the generation of CO₂. While single Bi₂MoO₆ performed satisfactory CO₂ and CO_x selectivity especially at very low SIE (74% CO₂ and 98% CO_x at 46 J/L), with a small decrease at higher SIE. When integrated as a hybrid catalyst, the mineralization of BMO-Mn exhibited a correlation with the increase of SIE, and reached an outstanding conversion of CO₂ (70%) and CO_x (99%) at 392 J/L. Fig. 3b displays the final carbon distributions for each of conditions. The results indicate that the hybrid catalyst not only enhanced the degradation of pollutant but also improved the mineralization of pollutant.

Further, the unknown carbon species in byproducts or deposited on the catalysts were analyzed by GC-MS (Fig. 3d, e and Table S2) and dynamic FT-IR spectroscopy (Fig. S4). The FT-IR results show that the main byproducts were acetic acid (C₂H₄O₂), acetone (C₃H₆O) and methane (CH₄) with others below the detectable limit. In GC-MS analysis, several intermediates containing NO₂, C₃H₆N₂O₇, C₂H₄O, CH₃NO₂, C₃H₆O, and others were detected both in the off-gas and on the surface of the catalyst, when pure MnO₂ was coupled with the plasma discharge. The results that most attracted our attention were the existence of NO₂ and several nitrate-containing intermediates. That means the addition of MnO₂ in the plasma discharge could facilitate the generation of NO_x from background reactions [27] and the generated NO_x would further react with some carbon-containing intermediates. While when BMO-Mn was used, only C₄H₈, CH₃NO₂ and C₃H₆O existed in the off-gas and C₄H₈, C₂H₄O and C₄H₈O were found on the surface of the catalyst with relatively weaker intensity. In addition, it was possible that the C₂H₄O was not a reaction byproduct and just came from the self-decomposition of EA during the 300 °C thermal desorption process, as demonstrated in the EA-TPD-MS experiments (Fig. S5). Therefore, it could be concluded that the BMO-Mn hybrid catalyst could effectively decrease the amount of intermediates and inhibit the generation of noxious compounds from background gas components.

In addition, activity cycling tests (Fig. 4a) and long-time tests (Fig. 4b) of BMO-Mn were carried out to investigate its stability. More than 95% EA removal efficiency could be obtained after both the 6 cycles of testing and the 35 h long-time tests. This result indicates that BMO-Mn has good stability for the catalytic degradation of EA. As well, the stability of the EA removal efficiency indicates that both components of this hybrid catalyst remained active throughout the tests, since such high efficiency could not be obtained for single Bi₂MoO₆ and solvo-MnO₂. However, the selectivity of CO_x decreased along with the cycles of testing and long-time test, indicating that the catalysts still has partially inactivated. Further, the time-course evolution of the amount of escaping O₃ was recorded in both situations, which exhibited an

evident rise along with reaction time. These results revealed that the ability of MnO₂ to degrade and utilize O₃ gradually decayed during the long time reaction, which was the main reason for the decrease of CO_x selectivity.

3.3. Investigation on possible synergistic mechanism

3.3.1. Relative dielectric constant, pore size and discharge intensity

A physical effect named the “packed bed effect” would be induced due to the occupation of the discharge gap and polarization effects on the surface of the pellets [4,5]. The original filamentary micro-discharge formed in a DBD reactor without packing would translate to a combination of localized filamentary discharge and surface discharges in the case of a packed bed [28]. This effect depends strongly on the contact angles, dielectric constant and the curvature of the pellets [29]. The catalysts' relative dielectric constants and their dielectric dissipation factors were investigated (Fig. 5), since the other two factors were kept constant. MnO₂ exhibited the largest value, while the other three catalysts exhibited smaller responses by orders of magnitude in both quantities, whose orders were as follows: BMO-Mn (2:1) > Solvo-MnO₂ > Bi₂MoO₆ for relative dielectric constant and Solvo-MnO₂ > BMO-Mn (2:1) > Bi₂MoO₆ for dielectric dissipation factor. The relative dielectric constant is characterized as the ability of a material to become polarized in an electric field, which would create a localized filamentary discharge, and result in an increase of overall electric field and electrons' energy at a range of 5–1000 [6]. While a higher dielectric constant (> 1000) of the packing material would cause a totally localized discharge and create an internal electric field opposed to the outside one, weakening the overall discharge [30]. Besides, packing catalysts of extremely high dielectric constant would inhibit the discharge at the contact points of the beads and even result in no surface discharge, which would limit the activation of catalysts in plasma due to the poor contact [6]. As well, it would lead to the generation of fewer O atoms and O₃ molecules [6]. That is to say, packing a catalyst with a relatively higher dielectric constant, but not too much higher, will favor the degradation of pollutants [31]. As for the dissipation factor, it represents the energy expended by heating when a material was under an applied electric field, and relatively lower values are desired [32]. It was revealed that the BMO-Mn hybrid catalyst exhibited a relatively higher dielectric constant and a lower dissipation factor, which facilitated the discharge process.

Furthermore, enhanced discharge near and inside the pores of mesoporous catalysts by the formation of microdischarge has also been reported by other researchers [33–35], and the pore size distribution of as-prepared samples were investigated as shown in Fig.S6. The results show that the nearly imperforate MnO₂ was transformed into a

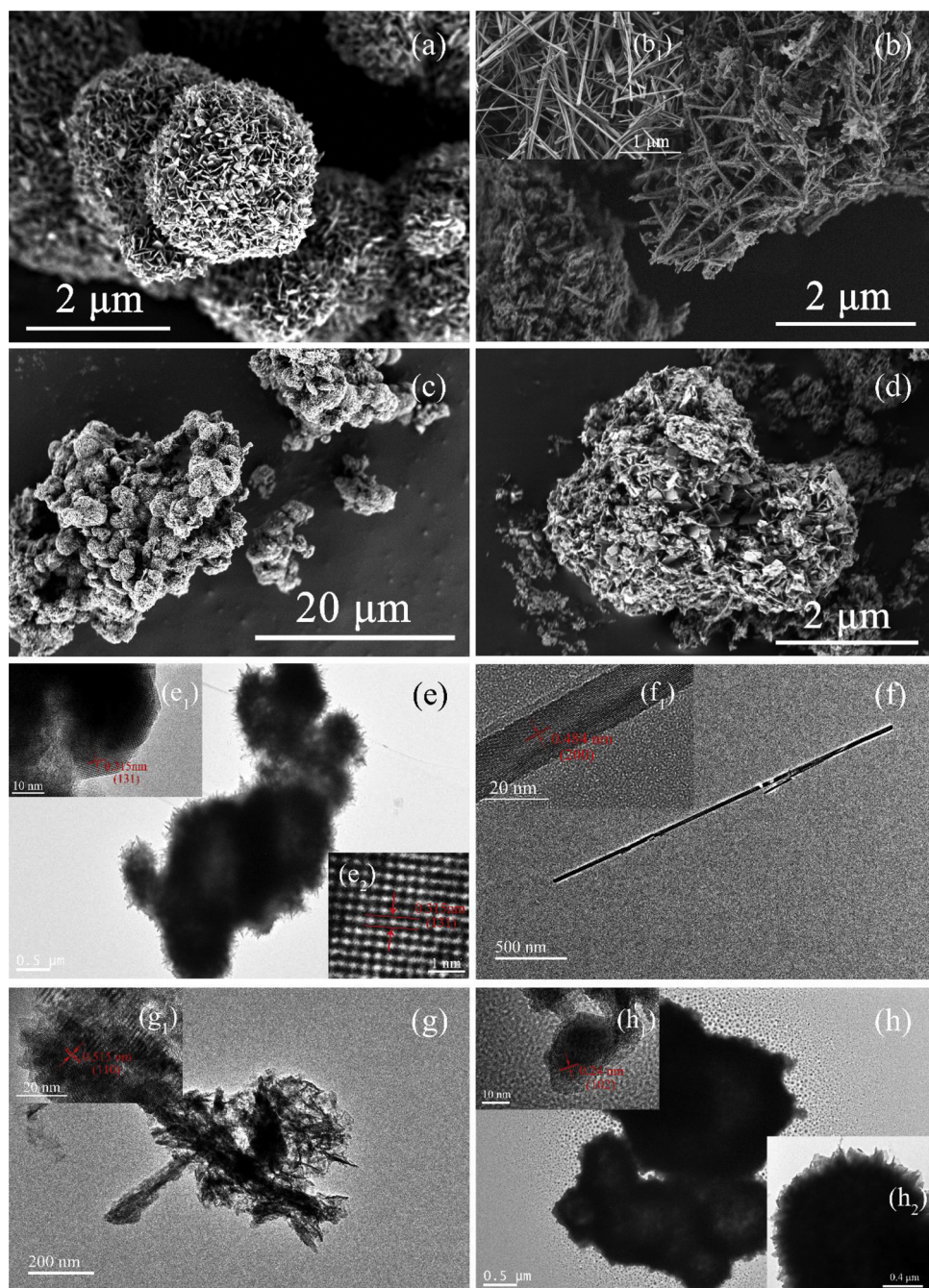


Fig. 2. Morphology characterization. SEM images of (a) flower-like Bi₂MoO₆, (b) Solvo-MnO₂, (b₁) MnO₂ nanowire, (c, d) Bi₂MoO₆/MnO₂(mole ratio 2:1). TEM images of (e) Bi₂MoO₆, (f) MnO₂ nanowire, (g) Solvo-MnO₂, (h) Bi₂MoO₆/MnO₂ (mole ratio 2:1).

structure of densely populated mesopores with a wide range of sizes after the solvothermal treatment, while the BMO-Mn composites showed regular mesopores with a diameter of 12.19 nm, in accordance with the TEM images. Since the pore size of 10 nm had been demonstrated to be the optimum in which the maximum electric field and electron density inside the pore could be obtained [35], the as-prepared catalysts packing in plasma allowed for the enhancement of discharge intensity.

Based on those two factors, the discharge intensity was characterized as a function of discharge current with different catalysts (Fig. S7), whose average current and effective current were also calculated in our utilization range (Fig. 6). Codirectional effects on both average current and effective current were induced by the packing of every catalyst. The results indicate that pure MnO₂ showed smaller values of average

current and effective current than the packing of glass balls, i.e., the inhibition of discharging was induced due to its excessively large dielectric constant. However, the discharge current showed an obvious increase for solvo-MnO₂ after the solvothermal treatment, which was attributed to the greatly decreased dielectric constant and enhanced amount of mesopores. Further, the hybrid catalyst (BMO-Mn) exhibited the densest discharge filaments due to its proper dielectric constant and pore size. Its average current increased by 129% and 23% compared with plasma alone and glass balls, respectively, at a modulated voltage of 35 V, while the effective current increased by 97.1% and 42.6%, corresponding to more high-energy electrons and active radicals. That was, an enhancement of the electric field in the plasma was achieved for this hybrid system, resulting in increased efficiency from the physical standpoint.

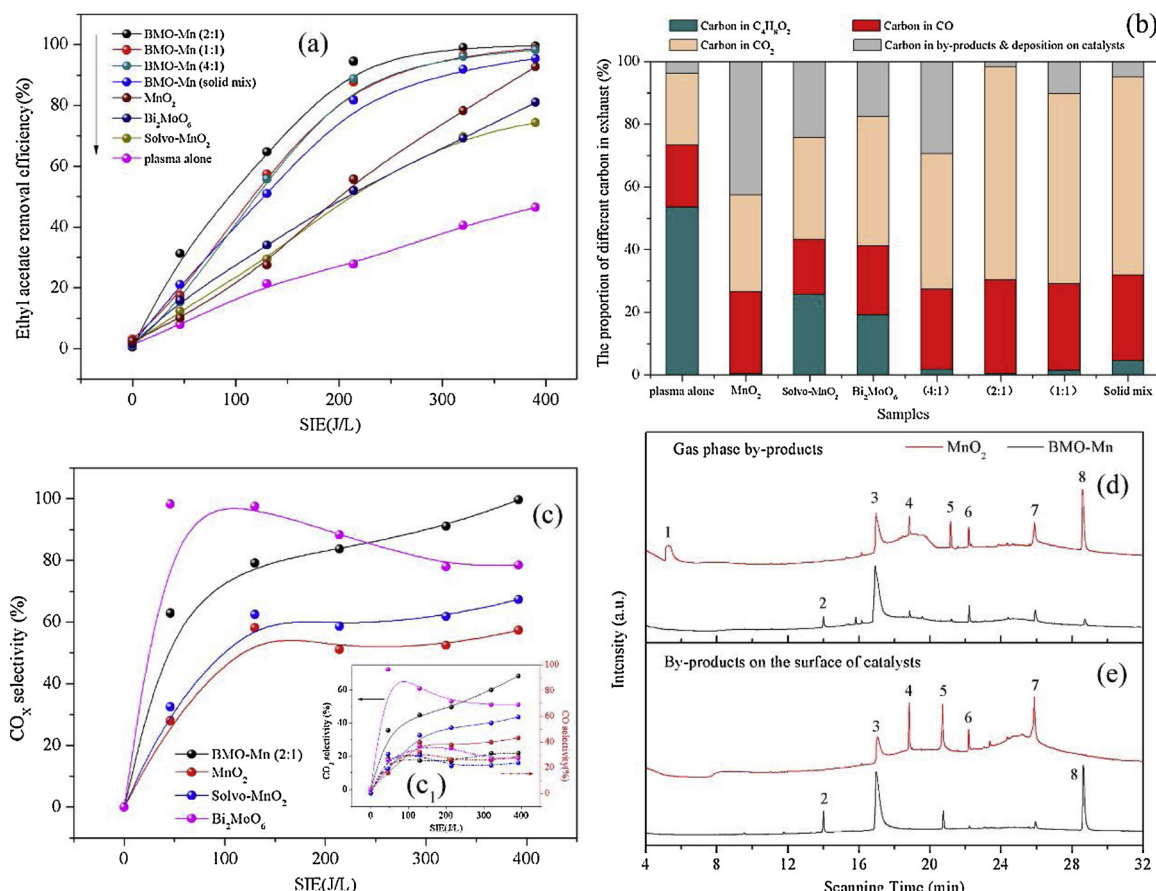


Fig. 3. Plasma-catalytic oxidation of EA. (a) EA degradation performance with SIE; (b) The proportion of different carbon in exhaust for different samples at SIE of 392 J/L; (c) CO_x selectivity for the as-prepared catalysts; (c₁) CO and CO₂ selectivity; (d) The gas phase by-products detected by GC-MS; (e) The by-products on the surface of catalysts detected by GC-MS.

3.3.2. BET, surface acidity, and adsorption capability for EA

The specific area and pore structure of all catalysts were calculated, as shown in Table S3. Notably, the S_{BET} of Solvo-MnO₂ (169.68 m²/g) exceeded all the other samples with the largest pore size and pore volume which are attributed to the solvothermal treatment. Although the intergrowth within Bi₂MoO₆ decreased the surface areas and blocked some mesopores, BMO-Mn still exhibited a mesoporous structure and a larger surface area than either single component and provided more active sites for the adsorption of EA.

The surface acidity of the as-prepared catalysts was investigated by NH₃-TPD (Fig. 7a), which is also known to make great contributions to the surface adsorption of EA [36,37]. All peaks were located at temperatures lower than 350 °C, solvo-MnO₂ exhibited a stronger peak of NH₃ desorption than pure MnO₂. While two evident peaks were

detected for Bi₂MoO₆ and BMO-Mn, BMO-Mn showed the stronger NH₃ desorption signal, indicating significant surface acidity.

Further, the adsorption capability of those catalysts for EA was measured (Fig. 7b) and the results were in accordance with the integrated effects of surface area and surface acidity. Solvo-MnO₂ showed small increase in the amount of adsorbed EA compared to pure MnO₂ due to its increased surface area and surface acidity. Together, the better surface acidity of Bi₂MoO₆ provided a satisfactory adsorption capability for EA. Furthermore, the combination of Bi₂MoO₆ and MnO₂ gave superior surface area and surface acidity to the hybrid catalyst, and the best adsorption capability was achieved. This facilitated the course of EA degradation, which was in line with the performance observed in the activity tests.

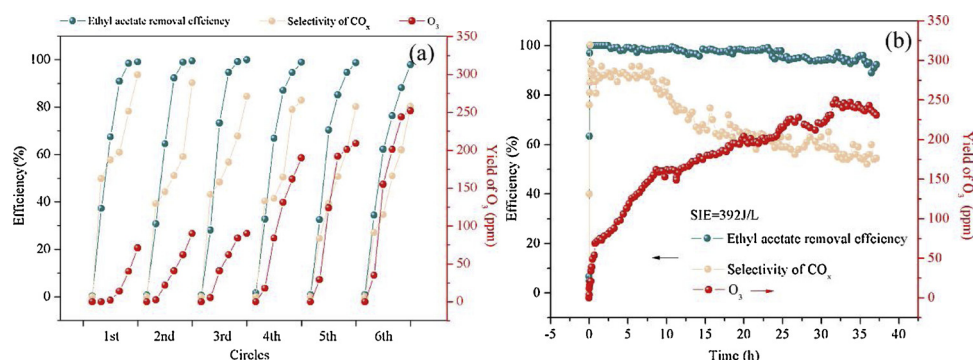


Fig. 4. The cycling tests against input energy (a) and long-time tests under an SIE of 392 J/L (b) of BMO-Mn (2:1).

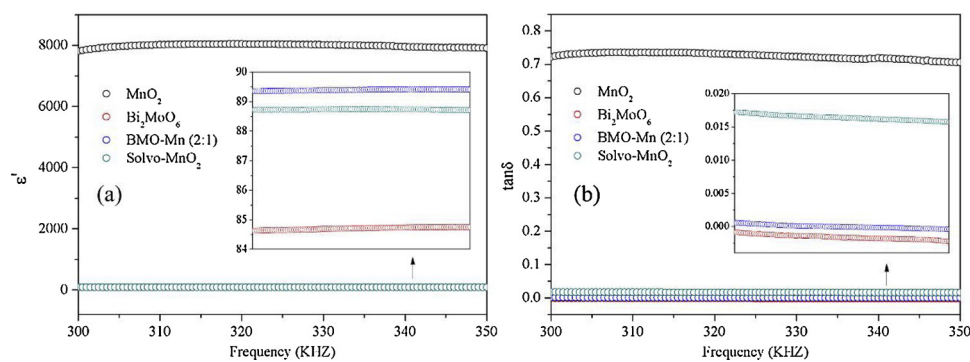


Fig. 5. The relative dielectric constant (a) and dielectric dissipation factor (b) of the as-prepared catalysts.

3.3.3. CO-PPR, single & synergistic effects, XPS, and oxidation property

CO plasma-programmed reduction (CO-PPR) was conducted to test the oxidation properties as displayed in Fig. 8, taking the yield of CO_2 (2361 cm^{-1}) [38] measured by FT-IR as the index signal. Samples who obtained higher yield of CO_2 in relatively lower SIE would be supposed to possess better oxidize ability. First of all, CO itself would be partly cracked to C and O radicals and re-transformed to CO_2 in the plasma, which was considered as the background value. The concentration of generated CO_2 displayed an evident increase at different SIE values after the participation of all catalysts, indicating that these catalysts could be all activated in plasma via different mechanisms. And the oxidation capability of the prepared catalysts, which was tested by CO-PPR, was found to increase in the following order: glass-balls < MnO_2 < solvo- MnO_2 < Bi_2MoO_6 < BMO-Mn(2:1) when the SIE was lower (90 and 214 J/L), but MnO_2 showed a huge upsurge at large SIE (392 J/L). That is to say, a higher input energy favors the oxidizability of MnO_2 . Besides, the solvothermal treatment was helpful for enhancing the oxidation capability of MnO_2 at low SIE, mainly due to the increased discharge intensity of the treated samples. The hybrid catalyst (BMO-Mn) possessed of the best oxidation capability under all conditions, which is in consistent with the activity test results.

For pure Bi_2MoO_6 , being an n-type semiconductor [24], its band structure was determined via UV-vis diffraction spectroscopy (UV-vis DRS) and valence band XPS (Fig. S8), implying a band gap energy (E_g) of 2.28 eV and a valence band (VB) of 1.91 eV . The conduction band (CB) was then estimated to be -0.37 eV . Bi_2MoO_6 could be activated by the collision of high-energy electrons in plasma (when the energy requirement was met) to produce the “electron (e^-) - hole (h^+) pairs”, which is called “pseudo photocatalysis” behavior [13]. Then, $\cdot\text{O}_2^-$ would be generated via the reaction of e^- and surface-adsorbed oxygen while $\cdot\text{OH}$ cannot be generated, since the E_{CB} of Bi_2MoO_6 was more negative than the O_2/O_2^- redox potential (-0.33 eV) [39] while the E_{VB} was lower than the OH^-/OH (1.99 eV) [40]. Experiments involving the addition of excess trapping agents ($\text{Na}_2\text{C}_2\text{O}_4$ [41] for h^+ and $\text{K}_2\text{Cr}_2\text{O}_7$

[42] for e^-) were carried out to clarify the role of e^- and h^+ (Fig. 9a and b), blank samples were shown in Fig. S9. These experiments showed that obvious enhancements of both the removal efficiency and CO_2 selectivity were obtained after the addition of $\text{Na}_2\text{C}_2\text{O}_4$, while the opposite results were found for the addition of $\text{K}_2\text{Cr}_2\text{O}_7$. That is, e^- and its derived species such as $\cdot\text{O}_2^-$ made the primary contribution to the reaction pathway, and especially to the CO_2 selectivity. Further, as reported, $\cdot\text{OH}$ may also be produced from the transformation of $\cdot\text{O}_2^-$ [43,44] as well as the plasma process [45], which plays a vital role for the degradation of pollutants. Hence, $\text{C}_7\text{H}_6\text{O}_3$ (trapping agents for $\cdot\text{OH}$) was added into Bi_2MoO_6 (Fig. 9a) and blank glass balls (Fig. S9) to clarify this mechanism. It was observed that EA removal efficiency experienced a dramatic decline in both situations, and in the case of Bi_2MoO_6 , it decreased even more than when $\text{K}_2\text{Cr}_2\text{O}_7$ was added, indicating that $\cdot\text{OH}$ was generated via these two pathways and occupied an important position. Considering that CO_x would be generated during the process of consuming $\cdot\text{OH}$ by $\text{C}_7\text{H}_6\text{O}_3$, further discussion of the influence of $\cdot\text{OH}$ on CO_x selectivity was ignored. In short, $\cdot\text{O}_2^-$ and its derived $\cdot\text{OH}$ played a leading role.

As demonstrated in the CO-PPR experiments, the oxidation capability of MnO_2 based on in traditional thermo-catalysis process [46,47] may also be expressed during the plasma process, with the addition of its good performance for the degradation and utilization of O_3 in plasma [16,17]. The variation of temperature of the DBD reactor during the reaction process was measured (Fig. S10a), and it was found to reach a peak of about 90°C , which may be not hot enough for the thermal activation of MnO_2 in its traditional thermo-catalysis process (Fig. S10b). But as reported, plasma is a system full of energy which could overcome thermodynamic barriers and enable reactions to occur at ambient temperature [48,49], as well as decrease some reaction temperatures [50]. Hence, it is suggested that the plasma discharge could activate the MnO_2 . For further verification, the performance of catalysts placed in the plasma zone and downstream of the plasma (this scheme is shown in Fig. S11) were compared and the results are

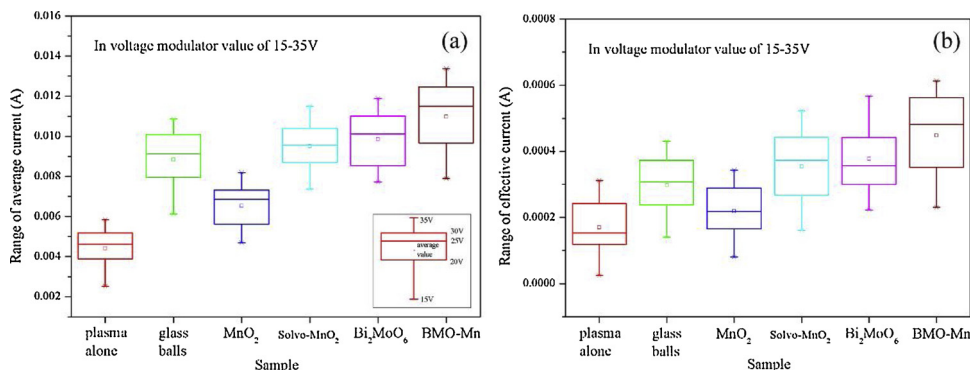


Fig. 6. The range of average current (a) and effective current (b) during the variation of the modulated voltage from 15 to 35 V under the conditions of plasma cooperating with different catalysts.

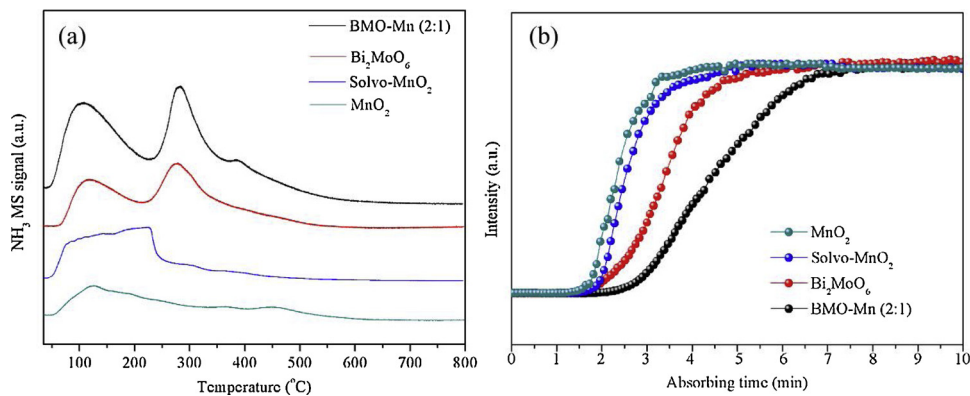


Fig. 7. NH₃-TPD MS signals (a) and the adsorption breakthrough curve of EA (b) of the as-prepared catalysts. Conditions of adsorption: 1000 ppm EA/He, 20 mL/min, 24 °C.

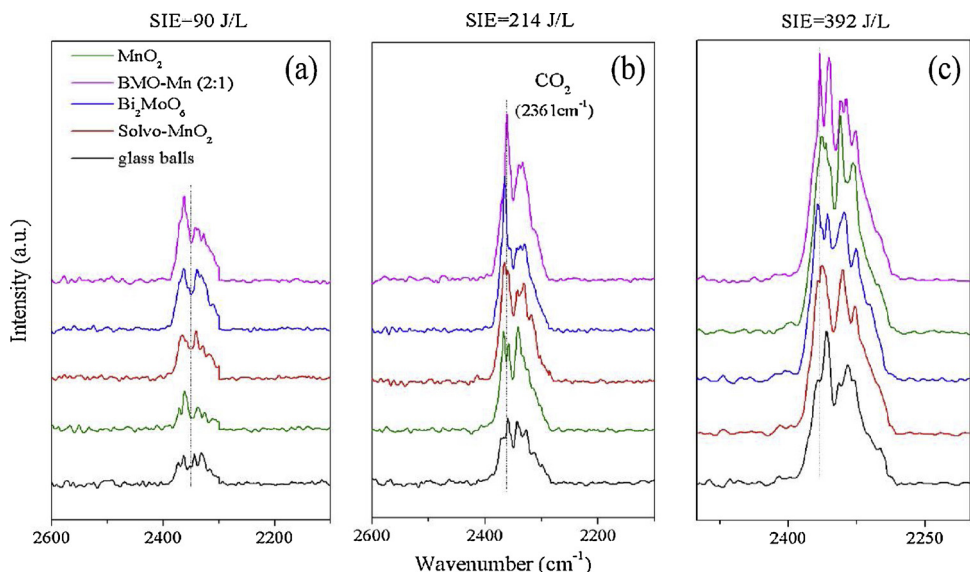


Fig. 8. CO plasma-programmed reduction (CO-PPR) for as-prepared catalysts at SIE of (c) 90 J/L, (d) 214 J/L and (e) 392 J/L.

displayed in Fig. 9c and d. For the case of catalysts placed downstream, gas first went through the plasma discharging zone packed with glass balls, and this outlet is denoted as Downstream-outlet 1. Then it flowed past the catalyst zone without discharging, and this outlet is denoted as Downstream-outlet 2. Nearly identical efficiency should be obtained from the in-plasma outlet and Downstream-outlet 2 if MnO₂ was only effective for the utilization of O₃. The removal efficiency for the situation of catalyst located in the plasma improved by about 20% compared to Downstream-outlet 2. That is to say, one more mechanism may exist when the catalyst is placed in the plasma. Besides, as mentioned above, the results of long-time tests and cycling tests showed the partial inactivation of the catalyst. The removal efficiency, which remained stable at around 95%, and the CO_x selectivity, which declined along with the amount of escaped of O₃, also revealed that the oxidation property of MnO₂ made a contribution.

In addition, the Eg and VB of BMO-Mn were demonstrated to be 2.23 eV and 1.82 eV, respectively (Fig. S8), thus its CB can be calculated to be -0.41 eV. Therefore, the “e-h⁺” pairs would be generated when the catalyst was activated by high-energy electrons in the plasma, and ·O₂⁻ and ·OH can be produced, as with Bi₂MoO₆. Experiments adding trapping agents were carried out for BMO-Mn as well (Fig. 9e and f), and essentially the same phenomena were observed. Just as with the Bi₂MoO₆ sample, e⁻ played a leading role. But it is worth mentioning that the removal efficiency and CO₂ selectivity were improved by about 10% at SIE of lower than 200 J/L if e⁻ were shielded (addition of

K₂Cr₂O₇), when compared to the sample of BMO-Mn sample. This phenomenon was not observed with pure Bi₂MoO₆, which suggests that h⁺ may have a new effect on composite catalysts and facilitate the degradation of pollutants. Since e⁻ were demonstrated to be the active center of Bi₂MoO₆ as mentioned, it is extremely possible that h⁺ lend a hand to the oxidizing capacity of MnO₂.

In order to clarify this assumption, XPS analyses with control experiments were conducted, as shown in Fig. 10. As is reported, the oxidation of VOCs by MnO₂ follows the Mars-van Krevelen (M-K) mechanism [51], and its activity is affected by its valence states [47], in which the higher oxidation state is preferable for the oxidation reaction [48]. Thus, it is critical for the course that the intermediate oxides (Mn₃O₄, Mn₂O₃, and MnO) are transformed back to MnO₂ in a timely manner [52]. For Mn 2p_{1/2} and Mn 2p_{3/2} (Fig. 10a and b), the peaks were deconvoluted to show a certain amount of Mn⁴⁺, Mn³⁺ and even Mn²⁺ (Table S4 shows their standard position), and the higher the concentration of high oxidation states, the higher the binding energy of the comprehensive peaks would be [47]. Initially, as for MnO₂, the two peaks were shifted to lower binding energy (about 1 eV) due to the solvothermal treatment (Solvo-MnO₂) when compared to pure MnO₂, indicating the decreased amount of Mn⁴⁺. This is the reason why lower removal efficiency was obtained for Solvo-MnO₂, especially at higher SIE. Then, considering the influence of the plasma discharge itself, a control experiment was conducted by discharging the catalysts in background atmosphere without the addition of EA (6% O₂/N₂, 214 J/

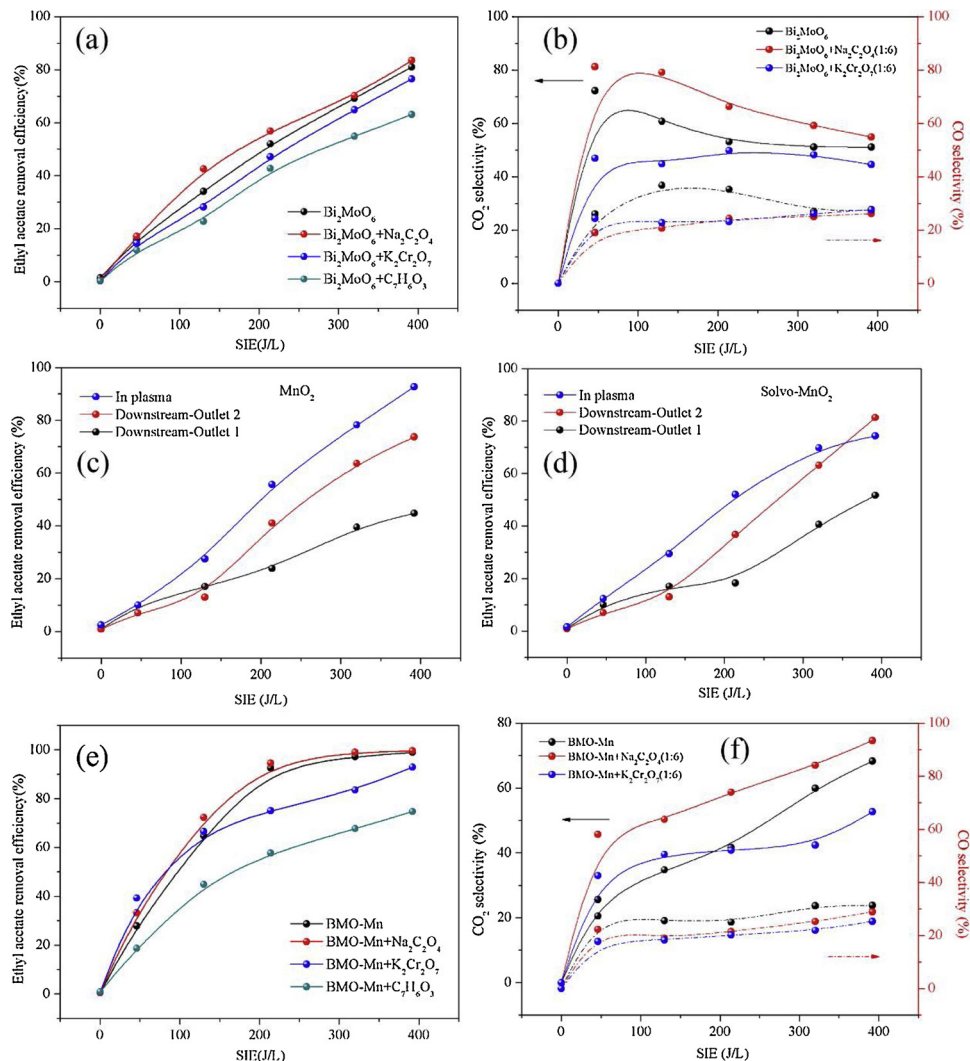


Fig. 9. (a) EA removal efficiency and (b) CO_x selectivity for Bi₂MoO₆ after the addition of trapping agents. Performance of catalysts placed in plasma zone and downstream of the plasma for (c) MnO₂ and (d) solvo-MnO₂. (e) EA removal efficiency and (f) CO_x selectivity for BMO-Mn(2:1) after the addition of trapping agents.

L, 2 h), and is denoted as “discharge treatment”. Comparing samples of fresh, used (after activity test (6% O₂/N₂, 200 ppm EA, 0–392 J/L)), and discharge treated MnO₂, a deviation (about 0.6 eV) to high binding energy was obtained when MnO₂ experienced a discharge treatment, while the deviation would fall to 0.3 eV after an activity test. This result reveals that the plasma discharge process favors the transformation of intermediate oxides back to MnO₂, and the oxidizing capacity of MnO₂

did make a contribution during the EA degradation reaction. When it comes to BMO-Mn, the shifts to higher binding energy were much more evident after both the activity test (about 1.0 eV) and the discharge treatment (about 1.9 eV). That is to say, the existence of Bi₂MoO₆ would allow the formation of Mn⁴⁺ under the plasma discharge, and h⁺ may well be the functional center as mentioned, which can suppress the recombination of e⁻ and h⁺ in return.

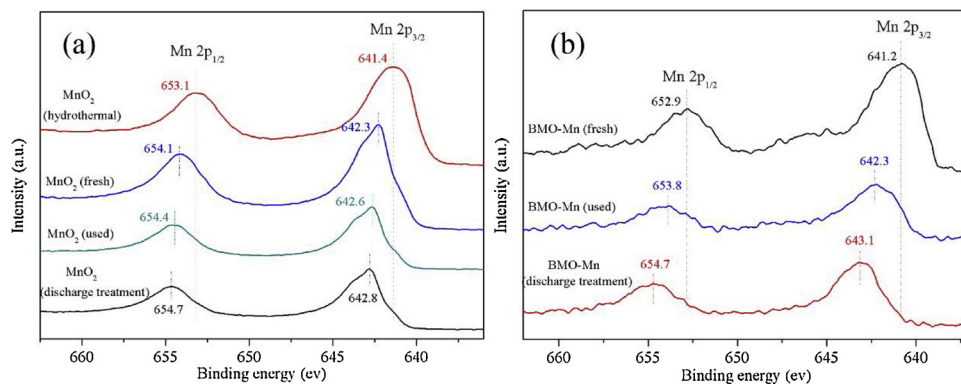


Fig. 10. The Mn 2p XPS spectra of (a) MnO₂ and sol-MnO₂ and (b) BMO-Mn (2:1) before use, after use, and after the discharge treatment. Condition of discharge treatment: 6% O₂/N₂, 214 J/L, 2 h.

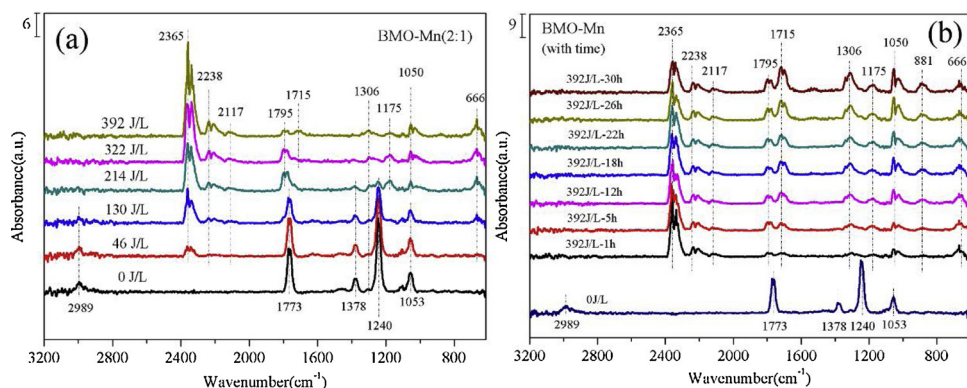


Fig. 11. Dynamic FT-IR study of the off-gas for BMO-Mn (2:1) with the increasing of (a) SIE and (b) test time at SIE of 392 J/L.

3.4. FT-IR and possible of pathways and mechanism

In order to clarify the reaction pathways and mechanism, dynamic FT-IR studies were performed (Fig. 11). The bands at 2989, 1773, 1378, 1240 and 1053 cm⁻¹ were ascribed to the infrared vibration of C—H from CH₂ and CH₃ stretching modes [53,54], ester carbonyl, bending symmetric CH₃(CO) vibration [54], the C—O stretching mode in the O = C—O group [55] and the stretching vibration of C—O—C [54], respectively, from EA. Firstly, all peaks for EA showed evident decline and even disappearance with the increase of input energy, under the conditions of plasma combined with BMO-Mn (Fig. 11a), along with the formation of CO₂ (2365 and 666 cm⁻¹) [38], CO (2117 cm⁻¹) [56], N₂O (2230 cm⁻¹) from plasma, monomeric acetic acid molecules in the gas phase (1795 and 1175 cm⁻¹) [57], acetone (1715 cm⁻¹ for stretching vibration of C=O), CH₄ (1306 cm⁻¹) [58] and O₃ (1050 cm⁻¹) [59], corresponding to the GC-MS results, with other by-products being beneath the detection limit of FT-IR spectroscopy. It could be deduced that acetic acid, acetone, and CH₄ acted as the main by-products. That is, the C—C and C—O bonds were likely to be broken to generate CH₃COO[·], CH₃CO[·], CH₃[·], and CH₃CH₂[·], followed by their further mineralization, due to the low dissociation energies of C—O (3.38 eV) and C—C (3.44 eV), along with C—H (4.29 eV) and C=O (7.55 eV) [60,61]. While in long-time tests (Fig. 11b), interesting phenomena were observed that the intensity of the peaks for acetic acid, acetone, CH₄, and O₃ showed clear increases with time, while the bands for CO₂ declined, demonstrating that the degradation and utilization of O₃ made a great contribution to the further oxidation of acetic acid, acetone, and CH₄, supporting the results of a previous study.

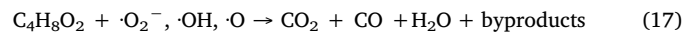
Based on these observations, an illustration of a possible synergistic mechanism for the degradation of EA was suggested, as shown in Fig. 12. Firstly, active radicals like O and N radicals were generated as well as electron-hole pairs (e[−]-h⁺) from Bi₂MoO₆ (when the energy was greater than its band gap) via the collision of high-energy electrons (e^{*}) from the plasma.



These e[−] would induce the generation of ·O₂^{·−} by reacting with surface-adsorbed oxygen, and ·O₂^{·−} are further transformed to ·OH, making a contribution to the degradation and mineralization of EA.



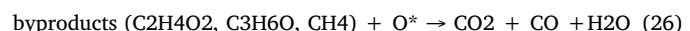
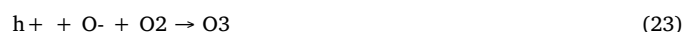
EA was initially transformed to CH₃COO[·], CH₃CO[·], CH₃[·], and CH₃CH₂[·], then further transformed to CH₃[·], CO₂, CO, due to the breaking of C—C and C—O bonds, resulting in CO₂, along with the generation of acetic acid, acetone and CH₄.



Meanwhile, MnO₂ also plays a part through its circulation of Mn⁴⁺, Mn³⁺ and even Mn²⁺. h⁺ generated from Bi₂MoO₆ would facilitate the generation of Mn⁴⁺, accelerating the oxidation of EA.



Apart from that, MnO₂ played the vital role of decomposing O₃ produced during this plasma course, being utilized especially for the mineralization of acetic acid, acetone and CH₄.



3.5. Extension to the degradation of other VOCs

To further investigate whether the catalyst of Bi₂MoO₆-MnO₂ was of universality for some other VOCs, several typical pollutants have been chosen for tests: Toluene, Acetone and P-xylene, as was displayed in Fig. 13. Highly enhanced degradation performance were obtained under the hybrid of plasma and BMO-Mn for the these VOCs compared with that of plasma alone (increased by 260% for Toluene, 209% for Acetone and 103% for P-xylene at the optimal condition), and more than 90% removal efficiency can be achieved at about 300 J/L for all selected VOCs, along with outstanding selectivity of CO and CO₂ (Fig. S12). Thus, it can be illustrated that this novel catalyst is universally applicable for the plasma-catalytic oxidation of VOCs.

4. Conclusion

MnO₂ and Bi₂MoO₆ were integrated for the first time as a hybrid catalyst (BMO-Mn), and combined with plasma discharge for the plasma-catalytic degradation of EA. The utilization efficiency of plasma species like e^{*}, O, and O₃ was highly enhanced in this hybrid system. Meanwhile, outstanding performance of nearly 100% removal

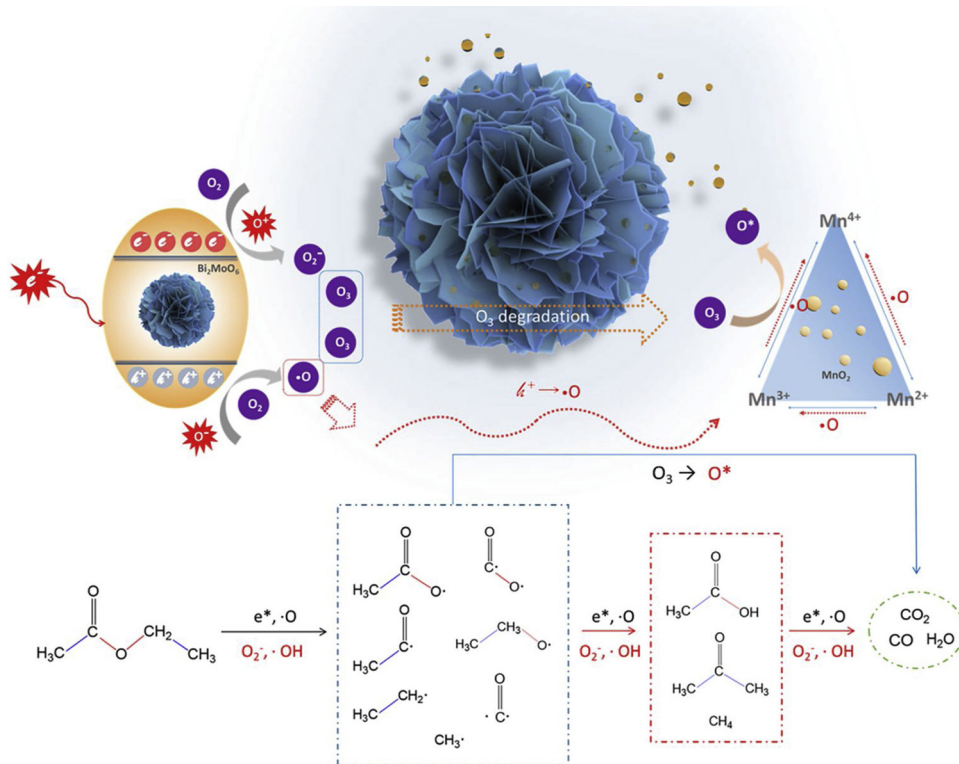


Fig. 12. Schematic diagram of the possible reaction pathways and mechanism.

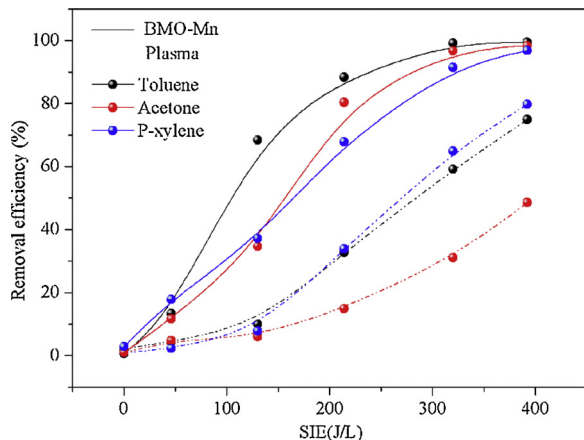


Fig. 13. Plasma-catalytic degradation of Toluene, Acetone and P-xylene.

efficiency as well as 70% selectivity of CO_2 and 99% selectivity of CO_x were achieved at SIE of 392 J/L in this hybrid system, which showed marked enhancement compared to using single catalyst or plasma alone. Synergetic effects among Bi_2MoO_6 , MnO_2 , and plasma were highlighted markedly in the discharge intensity of plasma, adsorption capability for EA, and oxidizing capability of the catalysts in plasma, all playing a part for the degradation and mineralization of EA. A mutual promotion between Bi_2MoO_6 and MnO_2 in the plasma was clarified by determining that h^+ from Bi_2MoO_6 facilitated the formation of Mn^{4+} , boosting the oxidation capability of MnO_2 . Thus, the recombination of e^- and h^+ was restrained in the hybrid system. As for the EA degradation pathways, it was demonstrated that acetic acid, acetone and CH_4 acted as the primary by-products in the hybrid system, and the decomposition and utilization of O_3 played a key role for the further mineralization of EA. In addition, the $\text{Bi}_2\text{MoO}_6\text{-MnO}_2$ catalysts were demonstrated to be universally applicable for the plasma-catalytic oxidation of other VOCs. It is expected that this work could provide a

refreshing perspective for future design of catalysts used in the “plasma-catalysis” system for the degradation of VOCs or other pollutants.

Acknowledgement

This work was financially supported by National Key Research and Development Program of China (2016YFC0204700), Zhejiang Provincial “151” Talents Program, Key Project of Zhejiang Provincial Science & Technology Program, the Program for Zhejiang Leading Team of S&T Innovation (Grant No. 2013TD07) and Changjiang Scholar Incentive Program (Ministry of Education, China, 2009).

Appendix A. Supplementary data

Supplementary material related to this article can be found, in the online version, at doi:<https://doi.org/10.1016/j.apcatb.2019.05.018>.

References

- [1] A.M. Harling, D.J. Glover, J.C. Whitehead, K. Zhang, Novel method for enhancing the destruction of environmental pollutants by the combination of multiple plasma discharges, Environ. Sci. Technol. 42 (2008) 4546–4550.
- [2] Q.H. Trinh, Y.S. Mok, Effect of the adsorbent/catalyst preparation method and plasma reactor configuration on the removal of dilute ethylene from air stream, Catal. Today 256 (2015) 170–177.
- [3] F. Holzer, U. Roland, F.D. Kopinke, Combination of non-thermal plasma and heterogeneous catalysis for oxidation of volatile organic compounds: part 1, Accessibility of the intra-particle volume, Appl. Catal. B-Environ. 38 (2002) 163–181.
- [4] A.M. Vandebroucke, R. Morent, N. De Geyter, C. Leyts, Non-thermal plasmas for non-catalytic and catalytic VOC abatement, J. Hazard. Mater. 195 (2011) 30–54.
- [5] J. Van Durme, J. Dewulf, C. Leyts, H. Van Langenhove, Combining non-thermal plasma with heterogeneous catalysis in waste gas treatment: a review, Appl. Catal. B-Environ. 78 (2008) 324–333.
- [6] W. Wang, H. Kim, K.V. Laer, A. Bogaerts, Streamer propagation in a packed bed plasma reactor for plasma catalysis applications, Chem. Eng. J. 334 (2018) 2467–2479.
- [7] Q. Zhang, W. Wang, A. Bogaerts, Importance of surface charging during plasma streamer propagation in catalyst pores, Plasma Sources Sci. T. 27 (2018) 065009.
- [8] H. Li, C. Liu, K. Li, H. Wang, Characterization and photocatalytic properties of

- nanoplate Bi₂MoO₆ catalysts, *J. Mater. Sci.* 43 (2008) 7026–7034.
- [9] B. Han, J. Zhang, P. Liu, J. Li, Y. Bian, H. Shi, Synthesis and luminescence properties of Eu³⁺ doped high temperature form of Bi₂MoO₆, *J. Electron. Mater.* 44 (2015) 1028–1033.
- [10] Y. Feng, H. Li, L. Ling, S. Yan, D. Pan, H. Ge, Z. Bian, Enhanced photocatalytic degradation performance by fluid-induced piezoelectric field, *Environ. Sci. Technol.* 52 (2018) 7842–7848.
- [11] Y. Zhang, M. Xu, H. Li, H. Ge, Z. Bian, The enhanced photoreduction of Cr (VI) to Cr (III) using carbon dots coupled TiO₂ mesocrystals, *Appl. Catal. B: Environ.* 226 (2018) 213–219.
- [12] W. He, Y. Sun, G. Jiang, Y. Li, X. Zhang, Y. Zhang, F. Dong, Defective Bi₄MoO₉/Bi metal core/shell heterostructure: enhanced visible light photocatalysis and reaction mechanism, *Appl. Catal. B: Environ.* 239 (2018) 619–627.
- [13] S. Chen, H. Wang, M. Shi, H. Ye, Z. Wu, Deep oxidation of NO by a hybrid system of plasma-N type semiconductor: High energy electron activated “pseudo photocatalysis” behavior, *Environ. Sci. Technol.* 52 (2018) 8568–8577.
- [14] J. Zhang, C. Niu, J. Ke, Ag/AgCl/Bi₂MoO₆ composite nanosheets: a plasmonic Z-scheme visible light photocatalyst, *Catal. Commun.* 59 (2015) 30–34.
- [15] T. Wang, S. Chen, H.Q. Wang, Z. Liu, Z.B. Wu, In-plasma catalytic degradation of toluene over different MnO₂ polymorphs and study of reaction mechanism, *Chinese J. Catal.* 38 (2017) 793–803.
- [16] W. Li, S.T. Oyama, Mechanism of ozone decomposition on a manganese oxide catalyst. 2. Steady-state and transient kinetic studies, *J. Am. Chem. Soc.* 120 (1998) 9047–9052.
- [17] B. Dhandapani, S.T. Oyama, Gas phase ozone decomposition catalysts, *Appl. Catal. B-Environ.* 11 (1997) 129–166.
- [18] H. Song, F. Hu, Y. Peng, K. Li, S. Bai, J. Li, Non-thermal plasma catalysis for chlorobenzene removal over CoMn/TiO₂ and CeMn/TiO₂: synergistic effect of chemical catalysis and dielectric constant, *Chem. Eng. J.* 347 (2018) 447–454.
- [19] Y. Feng, L. Ling, J. Nie, K. Han, X. Chen, Z. Bian, Z. Wang, Self-powered electrostatic filter with enhanced photocatalytic degradation of formaldehyde based on built-in triboelectric nanogenerators, *ACS nano* 11 (2017) 12411–12418.
- [20] M. Xu, Y. Chen, J. Qin, Y. Feng, W. Li, W. Chen, Z. Bian, Unveiling the role of defects on oxygen activation and photodegradation of organic pollutants, *Environ. Sci. Technol.* 52 (2018) 13879–13886.
- [21] X. Zhu, S. Zhang, Y. Yang, C. Zheng, J. Zhou, X. Gao, X. Tu, Enhanced performance for plasma-catalytic oxidation of ethyl acetate over La_{1-x}Ce_xCoO_{3+δ} catalysts, *Appl. Catal. B-Environ.* 213 (2017) 97–105.
- [22] G. Cheng, L. Yu, B. Lan, M. Sun, T. Lin, Z. Fu, X. Su, M. Qiu, C. Guo, B. Xu, Controlled synthesis of α-MnO₂ nanowires and their catalytic performance for toluene combustion, *Mater. Res. Bull.* 75 (2016) 17–24.
- [23] J. Tian, P. Hao, N. Wei, H. Cui, H. Liu, 3D Bi₂MoO₆ nanosheet/TiO₂ nanobelts heterostructure: enhanced photocatalytic activities and photoelectrochemistry performance, *ACS Catal.* 5 (2015) 4530–4536.
- [24] Y. Shimodaira, H. Kato, H. Kobayashi, A. Kudo, Photophysical properties and photocatalytic activities of bismuth molybdates under visible light irradiation, *J. Phys. Chem. B* 110 (2006) 17790–17797.
- [25] W. Shi, Y. Li, J. Hou, H. Lv, X. Zhao, P. Fang, F. Zheng, S. Wang, densely populated mesopores in microcuboid CeO₂ crystal leading to a significant enhancement of catalytic activity, *J. Mater. Chem. A* 1 (2013) 728–734.
- [26] X. Zhu, X. Tu, D. Mei, C. Zheng, J. Zhou, X. Gao, Z. Luo, M. Ni, K. Cen, Investigation of hybrid plasma-catalytic removal of acetone over CuO/γ-Al₂O₃ catalysts using response surface method, *Chemosphere* 155 (2016) 9–17.
- [27] J.L. Hueso, J. Cotrino, A. Caballero, J.P. Espinosa, A.R. Gonzalezelipe, Plasma catalysis with perovskite-type catalysts for the removal of NO and CH₄ from combustion exhausts, *J. Catal.* 247 (2007) 288–297.
- [28] X. Tu, H.J. Gallon, J.C. Whitehead, Electrical and spectroscopic diagnostics of a single-stage plasma-catalysis system: effect of packing with TiO₂, *J. Phys. D* 44 (2011) 482003.
- [29] W.S. Kang, J. Park, Y. Kim, S. Hong, Numerical study on influences of barrier arrangements on dielectric barrier discharge characteristics, *IEEE T. Plasma Sci.* 31 (2003) 504–510.
- [30] D. Mei, X. Zhu, Y. He, J.D. Yan, X. Tu, Plasma-assisted conversion of CO₂ in a dielectric barrier discharge reactor: understanding the effect of packing materials, *Plasma Sources Sci. T.* 24 (2014) 015011.
- [31] B.S.B. Patil, N. Cherkasov, J.E. Lang, A.O. Ihbadon, V. Hessel, Q.Q. Wang, Low temperature plasma-catalytic NO_x synthesis in a packed DBD reactor: effect of support materials and supported active metal oxides, *Appl. Catal. B-Environ.* 194 (2016) 123–133.
- [32] P.C. Joshi, M.W. Cole, Mg-doped Ba_{0.6}Sr_{0.4}TiO₃ thin films for tunable microwave applications, *Appl. Phys. Lett.* 77 (2000) 289–291.
- [33] K. Hensel, V. Martišovit, Z. Machala, M. Janda, M. Leštinský, P. Tardieu, A. Mizuno, Electrical and optical properties of AC microdischarges in porous ceramics, *Plasma Process. Polym.* 4 (2007) 682–693.
- [34] F. Holzer, F.D. Kopinke, U. Roland, Influence of ferroelectric materials and catalysts on the performance of non-thermal plasma (NTP) for the removal of air pollutants, *Plasma Chem. Plasma Process.* 25 (2005) 595–611.
- [35] Y. Zhang, H. Wang, Y. Zhang, A. Bogaerts, Formation of microdischarges inside a mesoporous catalyst in dielectric barrier discharge plasmas, *Plasma Sources Sci. T.* 26 (2017) 054002.
- [36] J.I. Gutiérrez-Ortiz, B. De Rivas, R. López-Fonseca, J.R. González-Velasco, Catalytic purification of waste gases containing VOC mixtures with Ce/Zr solid solutions, *Appl. Catal. B-Environ.* 65 (2006) 191–200.
- [37] S. Zuo, F. Liu, R. Zhou, C. Qi, Adsorption/desorption and catalytic oxidation of VOCs on montmorillonite and pillared clays, *Catal. Commun.* 22 (2012) 1–5.
- [38] I. Pitkanen, J. Huttunen, H. Halattunen, R. Vesterinen, Evolved gas analysis of some solid fuels by TG-FTIR, *J. Therm. Anal. Calorim.* 56 (1999) 1253–1259.
- [39] J. Li, X. Dong, G. Zhang, W. Cui, W. Cen, Z. Wu, F. Dong, Probing ring-opening pathways for efficient photocatalytic toluene decomposition, *J. Mater. Chem. A* 7 (2019) 3366–3374.
- [40] Y.J. Sun, Z.W. Zhao, F. Dong, W. Zhang, Mechanism of visible light photocatalytic NO_x oxidation with plasmonic Bi cocatalyst-enhanced (BiO)₂CO₃ hierarchical microspheres, *Phys. Chem. Chem. Phys.* 17 (2015) 10383–10390.
- [41] C.D. Jaeger, A.J. Bard, Spin trapping and electron spin resonance detection of radical intermediates in the photodecomposition of water at titanium dioxide particulate systems, *J. Phys. Chem.* 83 (1979) 3146–3152.
- [42] Z. Ai, J. Wang, L. Zhang, Substrate-dependent photoreactivities of BiOBr nanoplates prepared at different pH values, *Chinese J. Catal.* 36 (2015) 2145–2154.
- [43] F. Dong, Z. Wang, Y. Li, W. Ho, S.C. Lee, Immobilization of polymeric g-C₃N₄ on structured ceramic foam for efficient visible light photocatalytic air purification with real indoor illumination, *Environ. Sci. Technol.* 48 (2014) 10345–10353.
- [44] S. Gao, W. Cen, Q. Li, J. Li, Y. Lu, H. Wang, Z. Wu, A mild one-step method for enhancing optical absorption of amine-functionalized metal-organic frameworks, *Appl. Catal. B-Environ.* 227 (2018) 190–197.
- [45] T. Wang, S. Chen, H. Wang, Z. Liu, Z. Wu, In-plasma catalytic degradation of toluene over different MnO₂ polymorphs and study of reaction mechanism, *Chinese J. Catal.* 38 (2017) 793–803.
- [46] R. Xu, X. Wang, D. Wang, K. Zhou, Y. Li, Surface structure effects in nanocrystal MnO₂ and Ag/MnO₂ catalytic oxidation of CO, *J. Catal.* 237 (2006) 426–430.
- [47] K. Ramesh, L. Chen, F. Chen, Y. Liu, Z. Wang, Y. Han, Re-investigating the CO oxidation mechanism over unsupported MnO, Mn₂O₃ and MnO₂ catalysts, *Catal. Today* 131 (2008) 477–482.
- [48] L. Yu, X. Tu, X.D. Li, Y. Wang, Y. Chi, J.H. Yan, Destruction of acenaphthene, fluorene, anthracene and pyrene by a dc gliding arc plasma reactor, *J. Hazard. Mater.* 180 (2010) 449–455.
- [49] S. Paulussen, B. Verheyde, X. Tu, C. De Bie, T. Martens, D. Petrovic, A.A. Bogaerts, B. Sels, Conversion of carbon dioxide to value-added chemicals in atmospheric pressure dielectric barrier discharges, *Plasma Sources Sci. T.* 19 (2010) 034015.
- [50] A. Parastaei, W.F. Hoeben, B.E. van Heesch, N. Kosinov, E.J. Hensen, Temperature-programmed plasma surface reaction: an approach to determine plasma-catalytic performance, *Appl. Catal. B-Environ.* 239 (2018) 168–177.
- [51] V.D. Makwana, Y.C. Son, A.R. Howell, S.L. Suib, The role of lattice oxygen in selective benzyl alcohol oxidation using OMS-2 catalyst: a kinetic and isotope-labeling study, *J. Catal.* 210 (2002) 46–52.
- [52] S. Liang, F. Teng, G. Bulgan, R. Zong, Y. Zhu, Effect of phase structure of MnO₂ nanorod catalyst on the activity for CO oxidation, *J. Phys. Chem. C* 112 (2008) 5307–5315.
- [53] A.C. Pardal, S.S. Ramos, P.F. Santos, L.V. Reis, P. Almeida, Synthesis and spectroscopic characterisation of N-alkyl quaternary ammonium salts typical precursors of cyanines, *Molecules* 7 (2002) 320–330.
- [54] R.N. Oliveira, M.C. Mancini, F.C.S. De Oliveira, T.M. Passos, B. Quilty, R.M.S.M. Thire, G.B. Mcguinness, FTIR analysis and quantification of phenols and flavonoids of five commercially available plants extracts used in wound healing, *Materia-Brazil.* 21 (2016) 767–779.
- [55] J. Simonovic, J.S. Stevanic, D. Djikanovic, L. Salmen, K. Radotic, Anisotropy of cell wall polymers in branches of hardwood and softwood: a polarized FTIR study, *Cellulose* 18 (2011) 1433–1440.
- [56] J.A. Anderson, M.W. McQuire, C.H. Rochester, T. Sweeney, In situ FTIR study of CO/H₂ reactions over Rh/SiO₂ catalysts at high pressure and temperature, *Catal. Today* 9 (1991) 23–30.
- [57] L. Liao, C. Lien, J.L. Lin, FTIR study of adsorption and photoreactions of acetic acid on TiO₂, *Phys. Chem. Chem. Phys.* 3 (2001) 3831–3837.
- [58] P.G. Harrison, A. Torr, FT-IR study of the gas phase thermolysis of trimethylsilyl acetate, *J. Organomet. Chem.* 538 (1997) 19–29.
- [59] K. Skalska, J. Miller, S. Ledakowicz, Effectiveness of nitric oxide ozonation, *Chem. Pap.* 65 (2011) 193–197.
- [60] M.R. Nimlos, E.J. Wolfrum, M.L. Brewer, J.A. Fennell, G. Bintner, Gas-phase heterogeneous photocatalytic oxidation of ethanol: pathways and kinetic modeling, *Environ. Sci. Technol.* 30 (1996) 3102–3110.
- [61] C. Zheng, X. Zhu, X. Gao, L. Liu, Q. Chang, Z. Luo, K. Cen, Experimental study of acetone removal by packed-bed dielectric barrier discharge reactor, *J. Ind. Eng. Chem.* 20 (2014) 2761–2768.